Seasonally Stratified Analysis of Simulated ENSO Thermodynamics

Tomoki Tozuka, Jing-Jia Luo, Sébastien Masson, Toshio Yamagata

Seasonally Stratified Analysis of Simulated ENSO Thermodynamics

TOMOKI TOZUKA

Department of Earth and Planetary Science, Graduate School of Science, University of Tokyo, Tokyo, Japan

JING-JIA LUO

Frontier Research Center for Global Change/JAMSTEC, Kanagawa, Japan

SEBASTIEN MASSON

LOCEAN, Paris, France

TOSHIO YAMAGATA

Department of Earth and Planetary Science, Graduate School of Science, University of Tokyo, Tokyo, and Frontier Research Center for Global Change/JAMSTEC, Kanagawa, Japan

(Manuscript received 17 May 2006, in final form 2 February 2007)

ABSTRACT

Using outputs from the SINTEX-F1 coupled GCM, the thermodynamics of ENSO events and its relation with the seasonal cycle are investigated. Simulated El Niño events are first classified into four groups depending on during which season the Niño-3.4 sea surface temperature anomaly (SSTA) index (5°S–5°N, 120°–170°W) reaches its peak. Although the heat content of the tropical Pacific decreases for all four types, the tropical Pacific loses about twice as much during an El Niño that peaks during winter compared with one that peaks during summer. The surface heat flux, the southward heat transport at 15°S, and the Indonesian Throughflow heat transport contribute constructively to this remarkable seasonal difference. It is shown that the Indonesian Throughflow supplies anomalous heat from the Indian Ocean, especially during the summer El Niño–like event. Changes in the basic state provided by the seasonal cycle cause differences in the atmospheric response to the SSTA, which in turn lead to the difference between the surface heat flux and the meridional heat transport anomaly.

1. Introduction

The first law of thermodynamics is the basic principle in understanding the variability of climate system. For this reason, using a coupled GCM (CGCM), Tozuka et al. (2007) recently investigated the decadal variation of the tropical Indian Ocean through heat budget analysis. They revealed that the decadal modulation in the occurrence of the simulated Indian Ocean dipole (IOD; Saji et al. 1999) is mainly induced by variations in the southward Ekman heat transport across 15°S associated with the Mascarene high activities and variations in the Indonesian Throughflow related to the ENSO. As an extension, we have started examining origins of the decadal modulation of the ENSO based on heat budget analysis to shed a new light on this topic. The present work is the first step toward this direction and discusses seasonality of ENSO thermodynamics.

ENSO is the most dominant interannual air–sea coupled phenomenon, which has a significant impact on global climate [see Neelin et al. (1998) for an extensive review]. Among studies devoted to the understanding of ENSO based on thermodynamics, Wyrtki (1975, 1985) was the first to demonstrate that the warm water volume of the tropical Pacific tends to increase as a whole prior to an El Niño event, and then decreases during a course of the event. He calculated the warm water volume variability between 15°S and 15°N by integrating sea level variability obtained from tide gauges. This result was recently confirmed more pre-

Corresponding author address: Tomoki Tozuka, Department of Earth and Planetary Science, Graduate School of Science, University of Tokyo, 7-3-1 Hongo, Bunkyo-ku, Tokyo 113-0033, Japan.
E-mail: tozuka@eps.s.u-tokyo.ac.jp

DOI: 10.1175/JCLI4275.1

TABLE 1. Heat budget anomaly for five El Niño events in SODA Simple Ocean Data Assimilation (SODA; units: PW). Residual heat flux includes terms, such as the surface heat flux and vertical heat transport anomaly. HC is the upper-40-m heat content.

El Niño	Peak month	$\partial HC/\partial t$	Indonesian Throughflow	Heat transport (10°N)	Heat transport (15°S)	Residual
1982/83	December	−0.78	+0.39	−0.25	−0.27	−0.64
1986/87	July	−0.49	+0.19	−0.27	−0.06	−0.35
1991/92	March	−0.10	+0.73	0.07	−0.20	−0.70
1993	May	−0.10	+0.37	−0.05	−0.04	−0.37
1997/98	November	−1.10	+0.24	0.09	−0.89	−0.53

cisely by Holland and Mitchum (2003), who used the Ocean Topography Experiment (TOPEX)/Poseidon altimetry sea level data and OGCM results. Also, motivated by the earlier studies, Jin (1997) formulated the recharge–discharge oscillator paradigm. This is essentially the same with the earlier delayed oscillator paradigm that paid more attention to zonal redistribution of heat content anomalies (Schopf and Suarez 1988; Battisti and Hirst 1989). However, the recharge–discharge oscillator paradigm stresses the importance of the meridional heat transport associated with the off-equatorial Rossby waves, and many recent studies have been built upon it.

The above studies, however, do not discuss the role of the seasonal cycle. Rasmusson and Carpenter (1982) showed in their pioneering work that most ENSO events are closely linked to the annual cycle. However, the importance of the annual cycle in understanding ENSO events has long been dismissed. Several studies in the 1990s have revealed important roles played by the seasonal cycle in the irregularity, chaotic nature, and phase locking of ENSO events (Tziperman et al. 1994; Jin et al. 1994). More recently, Tozuka and Yamagata (2003) have shown that the ENSO may be interpreted as an interaction between the "interannual ENSO" mode and the "annual ENSO" mode. It is also shown that the interaction is susceptible to decadal changes. The seasonal signal may be responsible for the southward shift of the zonal wind stress anomaly that is considered to play a role in the decay of El Niño events (Harrison and Vecchi 1999; Lengaigne et al. 2006). Thus, we expect that investigating a seasonal modulation in the recharge–discharge process of ENSO will shed new light on understanding ENSO from a thermodynamical viewpoint.

Another feature to be understood about ENSO is related to differences among El Niño events. Based on the first appearance of a significant sea surface temperature anomaly (SSTA) in the Niño-3.4 region, Xu and Chan (2001) identified two types of El Niño events. One is called the spring type, where the SSTA first exceeds 0.5°C in April or May, and the other is called the summer type, where the SSTA does not become larger than this threshold until July or August. Horii and Hanawa (2004) further showed that the spring-type event is stronger and evolves more regularly. Although they explained the difference in terms of the western Pacific oscillator (cf. Weisberg and Wang 1997), its detailed mechanism was not given.

Using outputs from a 200-yr integration of a higher-resolution CGCM, we examine how the recharge–discharge process depends on the peak season of El Niño and why this dependence occurs. The paper is organized as follows. In the next section, we have analyzed the recharge–discharge process associated with El Niño in assimilation data. A brief description of the CGCM used in this study, along with its validity, is given in section 3. In section 4, we have calculated the heat budget of the tropical Pacific and constructed composite diagrams by classifying El Niño–like events into four groups based on the peak season. In particular, a detailed discussion on why the discharge process associated with these four types of El Niño–like events is so different is given. The final section is reserved for summary and discussions.

2. Recharge–discharge oscillator in an assimilation data

We have first analyzed an assimilation data prepared by Carton and Giese (2006, manuscript submitted to *J. Geophys. Res.*) by calculating the upper-440-m heat budget of the tropical Pacific between 10°S and 15°N. Five El Niño events that occurred after 1980 (1982/83, 1986/87, 1991/92, 1993, and 1997/98) are analyzed. Here, we use a reference temperature of 0°C in calculating the heat transport. The heat transport below 440 m is smaller compared with that of the upper 440 m and will not be discussed in the present study.

Interestingly, 1982/83 and 1997/98 El Niño events, which peak toward the end of the year, lose more heat compared with other El Niño events (Table 1). The largest contribution in heat discharge for 1982/83 El Niño comes from the residual heat flux, which includes

terms, such as the surface heat flux and vertical heat transport anomaly (−0.64 PW), and the meridional heat transport anomaly at both 10°N and 15°S also contributes to this heat loss by −0.25 and −0.27 PW, respectively. For the 1997/98 El Niño, the meridional heat transport anomaly at 15°S (−0.89 PW) and the residual heat flux anomaly (−0.53 PW) contribute to the large heat discharge. On the other hand, 1986/87 and 1993 El Niño events lose less heat mostly owing to the smaller negative anomaly in the residual heat flux and southward heat transport at 15°S. The large positive anomaly associated with the Indonesian Throughflow (+0.73 PW) during 1991/92 El Niño causes the tropical Pacific to fail to lose heat during El Niño.

However, because the number of events is limited, we cannot discuss statistical significance. Also, we cannot calculate a complete heat budget from the assimilation data because surface heat flux data are not given and temperature is restored to observations. Therefore, we analyze CGCM results with sufficiently long integration after validating the model performance against observation.

3. Model

a. Model description

The model data used in this study are obtained from an atmosphere–ocean–land CGCM run on the Earth Simulator. The model used is called SINTEX-F1 (Luo et al. 2003), which is an upgraded version of the SINTEX model (Guilyardi et al. 2003). The atmospheric component T106L19 ECHAM-4.6 (Roeckner et al. 1996) is coupled to the oceanic component Océan Parallélisé (OPA) 8.2 (Madec et al. 1998) using the coupler Ocean, Atmosphere, Sea Ice, and Soil (OASIS) 2.4 (Valcke et al. 2000). The SINTEX model of Guilyardi et al. (2003) and the SINTEX-F1 model used in this study are different in many aspects. One major difference is that atmospheric component of Guilyardi et al. (2003) is T30, whereas that in the SINTEX-F1 is T106. As a result, the skill of simulating ENSO has been improved significantly. For instance, the major weakness of the SINTEX model of Guilyardi et al. (2003) was that the Niño-3 SSTA spectrum showed very strong peak at 2-yr period, whereas the SINTEX-F1 model is successful in reproducing 4-yr periodicity in ENSO (Luo et al. 2003; Guilyardi et al. 2004). The horizontal resolution of the OGCM in the SINTEX-F1 model is 2° × 2°, with an increased meridional resolution up to 0.5° near the equator. There are 31 levels in the vertical with 19 levels in the upper 400 m. The coupling information is exchanged every two hours between the atmospheric and oceanic components and no measures for flux adjustments are taken. The five-daily output from the last 200 yr of the total 220-yr model integration is used for analysis after removing a linear trend using a least squares fit. More details of the CGCM can be found in the above references.

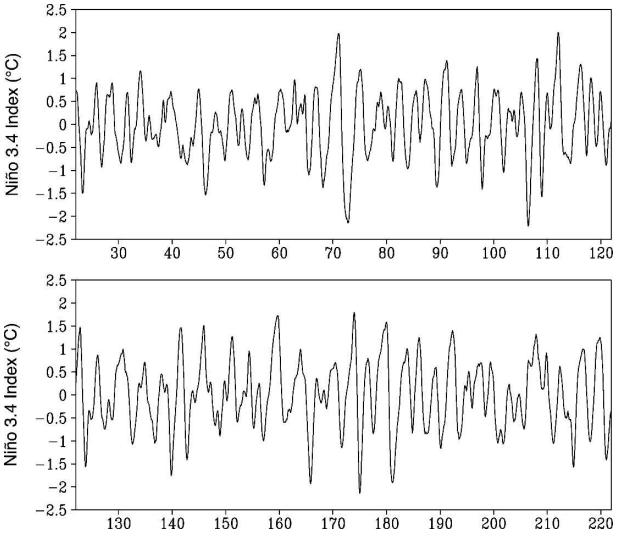

FIG. 1. Time series of five-month running mean Niño-3.4 index in the SINTEX-F1 model.

b. Model validation

It is necessary to check the validity of the present model results prior to analyzing thermal variations in the tropical Pacific associated with the ENSO. The simulated seasonal air–sea interaction in the tropical Pacific, or the annual ENSO, is investigated in detail by Tozuka et al. (2005) and will not be repeated here. In brief, many features of the annual ENSO, such as the classical El Niño that initiates the air–sea interaction in the eastern equatorial Pacific, the westward expansion of the seasonal SSTA, and the westward propagation of the seasonal SSHA along 5°N, are well reproduced in the model.

Figure 1 shows the Niño-3.4 (5°S–5°N, 120°–170°W) index, which is used to define El Niño–like events in the present study. Note that Niño-3.4 SSTA is calculated by simply subtracting the monthly mean climatology, because the modulation in the annual cycle is very small in the Niño-3 region as well as the Niño-3.4 region (Tozuka et al. 2005), and the result presented here is not sensitive to the way in which it is calculated (cf. Pezzulli et al. 2005). This is because the simulated interaction between the seasonal air–sea interaction and the interannual ENSO was much weaker because the meridional expansion of the seasonal SSTA to the north of the equator is not well reproduced in the eastern tropical Pacific (Tozuka et al. 2005).

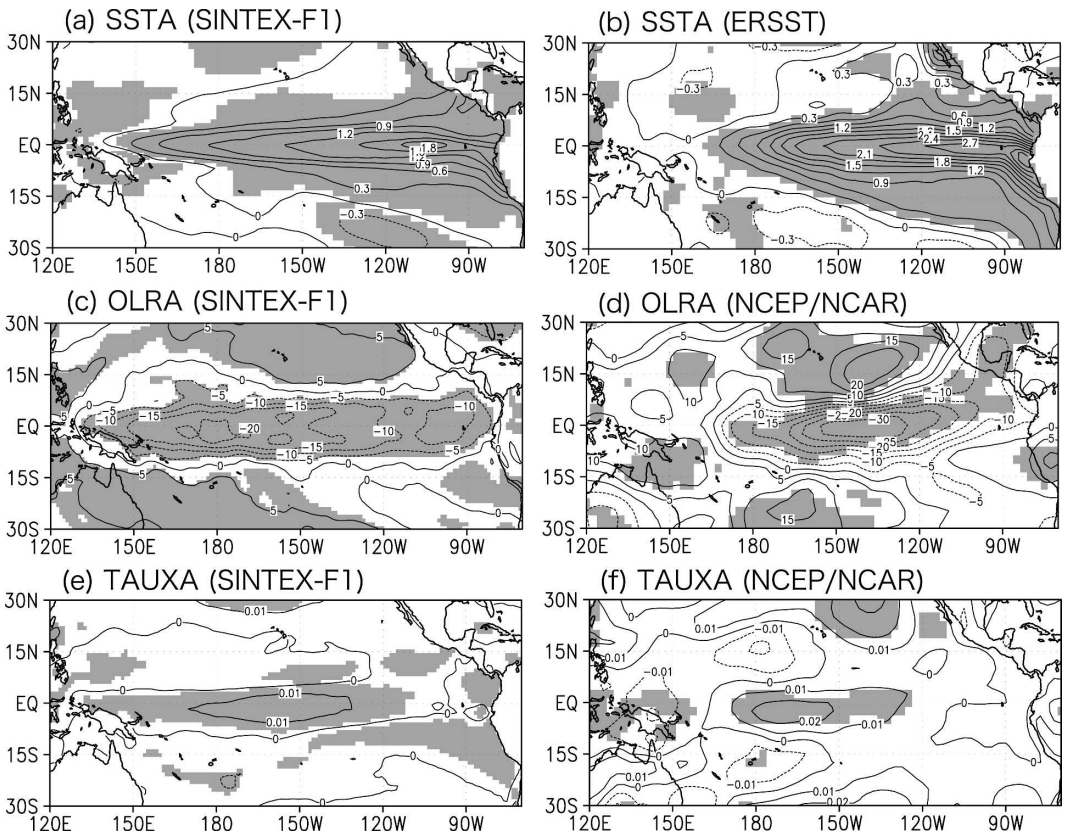

FIG. 2. Composite diagrams of (a),(b) SSTA, (c),(d) OLRA, and (e),(f) TAUXA for (left) SINTEX-F1 model and (right) observation/reanalysis data. Units are in °C, N m^{-2}, and W m^{-2}, respectively. The statistical significance of the anomalies is estimated by the two-tailed *t* test. Shading indicates anomalies exceeding 95% confidence level.

To extract common features of simulated warm events, composite diagrams of SSTA, outgoing longwave radiation anomalies (OLRA), and zonal wind stress anomaly at the peak phase are constructed (Fig. 2). Here, El Niño–like events are selected according to a criterion that the Niño-3.4 index with a five-month running mean exceeds 0.8°C for at least three consecutive months. For observation, five warm events that occurred after 1980 (1982/83, 1986/87, 1991/92, 1993, and 1997/98) are used. We used SST data from Smith and Reynolds (2003) and wind stress and outgoing longwave radiation (OLR) data from the National Centers for Environmental Prediction–National Center for Atmospheric Research (NCEP–NCAR) reanalysis project (Kalnay et al. 1996). Because the positive SSTA extends too far to the west as seen in all other CGCMs, the negative OLRA also extends far into the western Pacific. The westerly wind stress anomaly is seen along the equator, indicative of a weakened Walker circulation, but the anomaly again extends into the far western Pacific for the same reason. The amplitude of the anomalies is stronger for the observation; the peak in SSTA, OLRA, and zonal wind stress anomaly (TAUXA) in the equatorial region between 150°E and 90°W are 1.9°C (2.8°C), −24 W m^{-2} (−35 W m^{-2}), and 0.015 N m^{-2} (0.026 N m^{-2}) in the model (observation), respectively. However, we note that two warm events included in composites for observation are the strongest El Niño events of the past century, explaining the discrepancy to some extent. In summary, many features during the peak phase of warm events are relatively well reproduced in the CGCM, except for the stronger westward extension of the anomalies [also see Achuta-Rao and Sperber (2006) and Guilyardi (2006) for the skill of the Intergovernmental Panel on Climate Change (IPCC) fourth assessment report (AR4) models in simulating ENSO].

Next, monthly standard deviation of the simulated Niño-3.4 is compared with that calculated from the Extended Reconstructed Sea Surface Temperature (ERSST) to see whether the nature of ENSO events approximately locked to the seasonal cycle is reproduced in the model (Fig. 3). Although the seasonal variation of the simulated standard deviation is smaller,

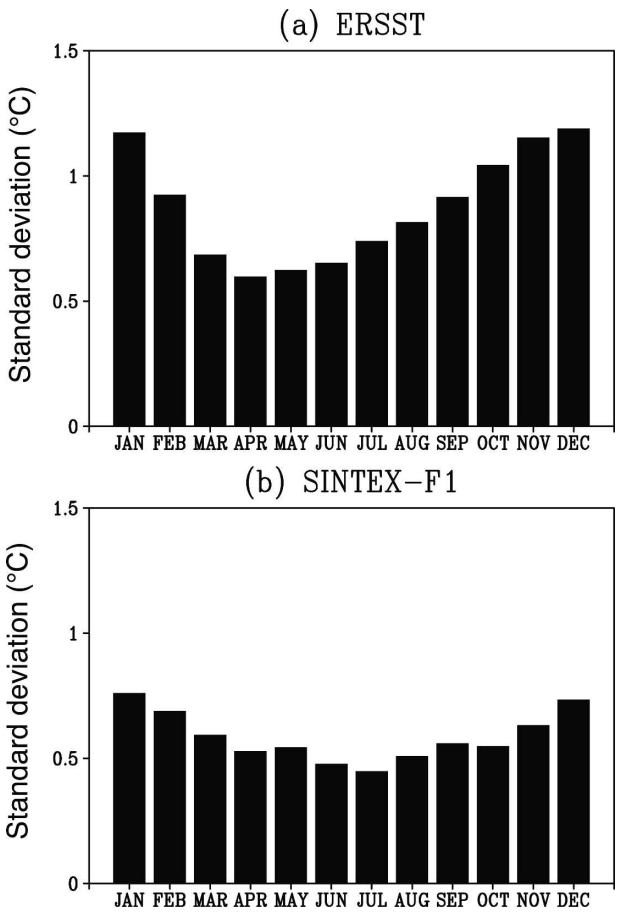

FIG. 3. Histograms of monthly std dev for Niño-3.4 index (°C) for (a) observations and (b) the SINTEX-F1 model.

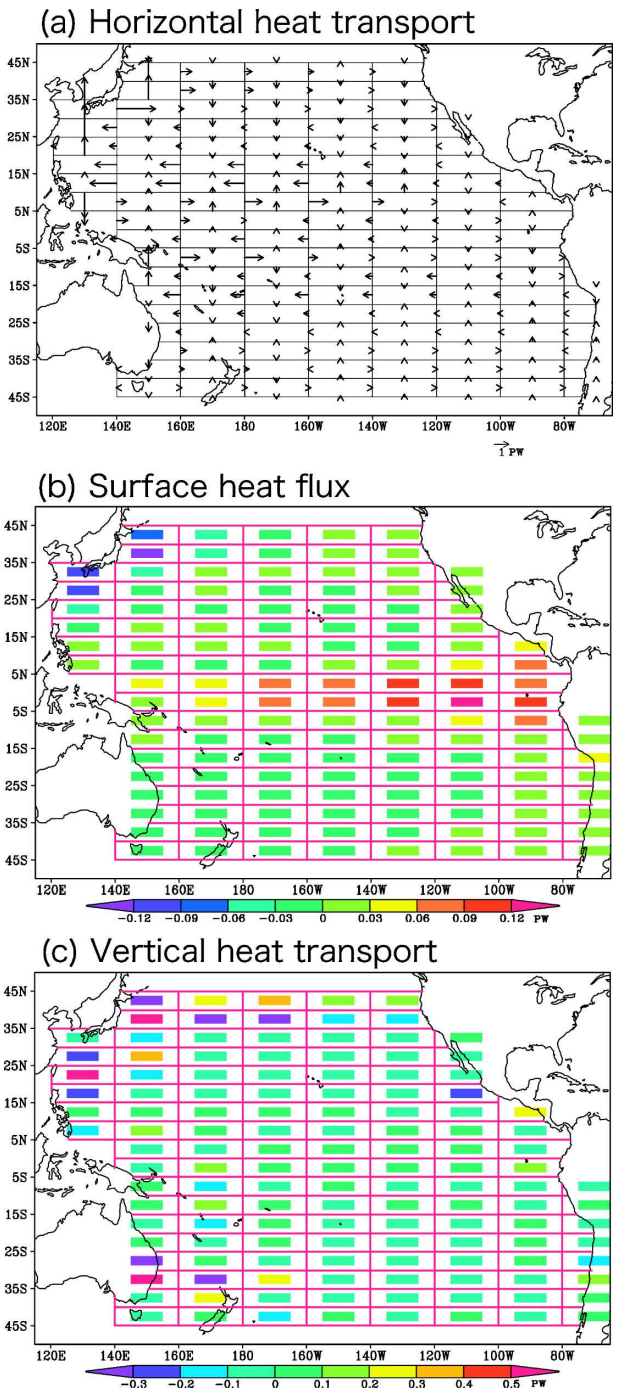

FIG. 4. Annual mean heat budget of the Pacific: (a) horizontal heat transport, (b) surface heat flux, and (c) vertical heat transport at 440-m depth.

the model is successful in capturing the peak in boreal winter.

Given that SINTEX-F1 has relatively good skill in simulating climate variability in the Tropics, including ENSO and IOD (see also Luo et al. 2003; Tozuka et al. 2005), we expect that the model can provide useful insight into the climate variability in the tropical Pacific.

4. Recharge–discharge oscillator in the CGCM

a. Annual mean heat budget

We have first divided the Pacific Ocean into 132 boxes as shown in Fig. 4, and calculated an annual mean heat budget for each box (cf. Philander and Pacanowski 1986). As is well known, the ocean gains heat in the equatorial cold tongue and loses heat in the western boundary current regions of the Kuroshio Extension and the East Australian Current (cf. Boccaletti et al. 2004). Those regions of heat gain and loss must be connected somehow to keep the ocean in a steady thermal balance; heat must be transported from the cold tongue region to the western boundary current regions. In the Northern Hemisphere, the heat absorbed near the equator is transported to the north by the Ekman transport, owing to the northeasterly trade winds. Then, the

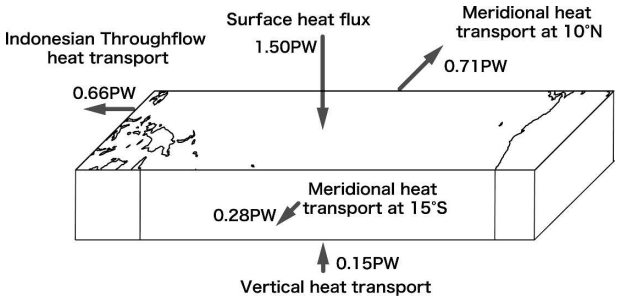

FIG. 5. Schematic diagram of the annual mean heat budget of the tropical Pacific for the upper 440 m.

heat is advected westward between 10° and 25°N by the North Equatorial Current (NEC). After reaching the western boundary, the heat is partly returned to the equatorial region by the Mindanao Current and the rest is transported farther northward by the Kuroshio, where a large amount of heat is released to the atmosphere above the Kuroshio Extension. In the Southern Hemisphere, the heat absorbed near the equator is first transported southward by the Ekman transport linked with the southeasterly trade winds and then westward by the South Equatorial Current. This heat is partly transported back to the equatorial region by the New Guinea Coastal Current and partly transported poleward by the East Australian Current. Within the equatorial region, the heat is redistributed mainly by the North Equatorial Countercurrent, the South Equatorial Current, and the Equatorial Undercurrent. The above features are in agreement with the large-scale circulation in the Pacific depicted by Reid (1997).

The annual mean heat budget in the Tropics may be summarized with the schematic diagram of Fig. 5. The tropical Pacific gains 1.50 PW from the atmosphere, and 0.15 PW from the deeper layer, while it loses 0.66 PW from the Indonesian Throughflow, and 0.71 PW (0.28 PW) by the northward (southward) heat transport across 10°N (15°S). These values resulting from the meridional heat transport and the Indonesian Throughflow are within the range of observed estimates (e.g., Talley 2003) and an OGCM constrained by the World Ocean Circulation Experiment (WOCE) data (e.g., Stammer et al. 2003).

b. *Seasonal modulation of the recharge–discharge oscillator*

To examine how the annual mean picture of the heat budget is altered by ENSO-like interannual events, we have constructed composite diagrams after classifying simulated events into four groups depending on the season [December–February (DJF): winter, March–May (MAM): spring, June–August (JJA): summer, and September–November (SON): fall] in which the Niño-3.4 SSTA reaches its peak (Fig. 1). As shown in Table 2, out of 43 warm events, 17, 8, 8, and 10 events reach their maximum strength in winter, spring, summer, and fall, respectively. The fact that the El Niño–like event reaches its peak often in boreal winter is consistent with the observation, suggesting that the model is relatively successful in reproducing the phase-locking nature to the annual cycle (Tozuka et al. 2005). Although we have analyzed all four types, we focus on the winter and summer El Niño in the rest of this study, because these are two extremes.

TABLE 2. Number of El Niño events that reaches their maximum strength.

Season	Winter (DJF)	Spring (MAM)	Summer (JJA)	Fall (SON)
Events	17	8	8	10

Figure 6 shows anomalies in the rate of change in the heat content, the surface heat flux, the Indonesian Throughflow, and the meridional heat transport at 15°S and 10°N. Although the tropical Pacific loses heat in both cases, their magnitude is surprisingly different. In fact, the heat loss during the "winter El Niño" is about two times larger than that of the "summer El Niño." The winter El Niño is more efficient in losing heat accumulated in the tropical Pacific. This is in agreement with our analysis in section 2. The next question then is what causes this difference. We are also interested in how each component varies during the course of the event.

From Fig. 7, we see that the model heat content decreases during the El Niño–like events with the heat content anomaly leading Niño-3.4 by eight (seven) months for the winter (summer) El Niño–like event (Figs. 7a–d). This is in good agreement with observation (Meinen and McPhaden 2000), suggesting that the present model is also very successful in capturing this important relationship between the SSTA and equatorial heat content anomaly associated with El Niño. We note that Niño-3.4 SSTA becomes –0.84°C (−0.30°C) one year after the peak of winter (summer) El Niño. This suggests that the summer El Niño–like event discussed in this study differs from the "aborted" events discussed in Guilyardi et al. (2003), but is more closely related to the summer- or summer–fall-type El Niño (cf. Xu and Chan 2001; Horii and Hanawa 2004).

The Indonesian Throughflow advects less heat compared to the climatology (i.e., supplies anomalous heat

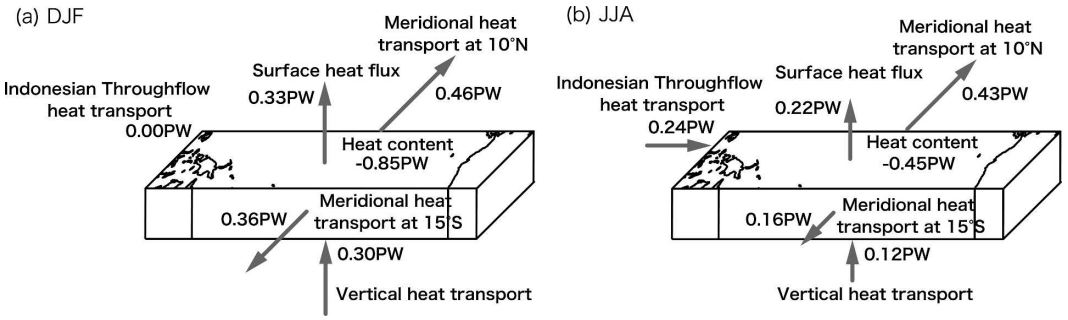

FIG. 6. Composite diagrams of anomalies in the rate of change of heat content, surface heat flux, Indonesian Throughflow, and meridional heat transport at 15°S and 10°N. The values are averaged over nine months centered around the peak in (a) winter and (b) summer El Niño–like events. All anomalies other than the Indonesian Throughflow heat transport anomaly during the winter El Niño–like events are statistically significant at 95% confidence level when tested with the *t* test.

from the Indian Ocean) during El Niño–like events (cf. Meyers 1996; England and Huang 2005), especially during the summer type (Fig. 6). The heat transport anomaly becomes negative just after the peak during the winter El Niño, while it remains positive over four months after the peak during the summer El Niño (Figs. 7g,h). This is why the heat transport anomaly over a 9-month period becomes 0.00 PW (0.24 PW) during the winter (summer) El Niño–like events (Fig. 6). However, one common feature between the winter and summer El Niño–like events is that the peak in the negative heat transport anomaly occurs in February after the peak in the Niño-3.4 index (Figs. 7g,h). This is explained by the negative SSHA in the eastern Indian Ocean, which is associated with the IOD. As shown in Fig. 8, a positive IOD sometimes co-occurs with an El Niño–like event, and peaks toward the end of a year. Thus, the IOD events may affect the heat budget of the tropical Pacific through the oceanic route (cf. Masumoto 2002). The influences of the tropical Indian Ocean on the tropical Pacific through the atmosphere have been discussed in previous studies (e.g., Kug and Kang 2006). However, no study to date has pointed out this Indian Ocean influence on the Pacific ENSO events.

In Fig. 9, we compare the magnitude of four components of surface heat flux anomalies during the peak phase of El Niño–like events, when surface heat flux anomalies are statistically significant for both cases (Figs. 7e,f). The largest contribution comes from the shortwave radiation, which is mostly concentrated in the equatorial band between 5°S and 5°N (figure not shown). The seasonal difference, which is statistically significant at the 95% confidence level when tested with the *t* test, is related to the convective activity associated with warm events. The area-averaged vertical speed anomaly at 500 hPa in the equatorial band (5°S–5°N) is –0.016 Pa s^{-1} for the winter El Niño–like event and –0.010 Pa s^{-1} for the summer El Niño–like event. Because the peak SSTA associated with the winter El Niño is 0.3°C warmer, the anomaly is larger. The background seasonal SST (Tozuka and Yamagata 2003) may also contribute to this difference. These results support the finding using an intermediate coupled model by Tziperman et al. (1997), who showed that the wind divergence field associated with the atmospheric heating is the most dominant seasonal effect to ENSO. On the other hand, the longwave radiation and the latent heat flux anomalies have smaller contributions because of their smaller seasonal dependence (the difference is below 95% confidence level for latent heat flux anomaly). The sensible heat flux anomaly is negligible for both cases.

Figure 10 shows details of the meridional heat transport anomaly. The southward heat transport anomaly across 15°S is larger for the winter El Niño–like events (Fig. 10b). This is mostly due to the 0.2-PW difference in the Ekman transport anomaly. The northward heat transport anomaly at 10°N is slightly stronger for the winter El Niño–like events, but the difference is not statistically significant. The Ekman heat transport and interior geostrophic anomalies (only significant at the 80% confidence level) show a larger contribution in discharging heat during the winter El Niño–like events. However, the western boundary current contributes negatively to the discharge during El Niño–like events and it is larger during the winter El Niño–like events. Because the bifurcation latitude of the NEC moves northward during most El Niño–like events, the equatorward heat transport by the Mindanao Current increases and returns heat to the equatorial belt. This relation between the western boundary current and the

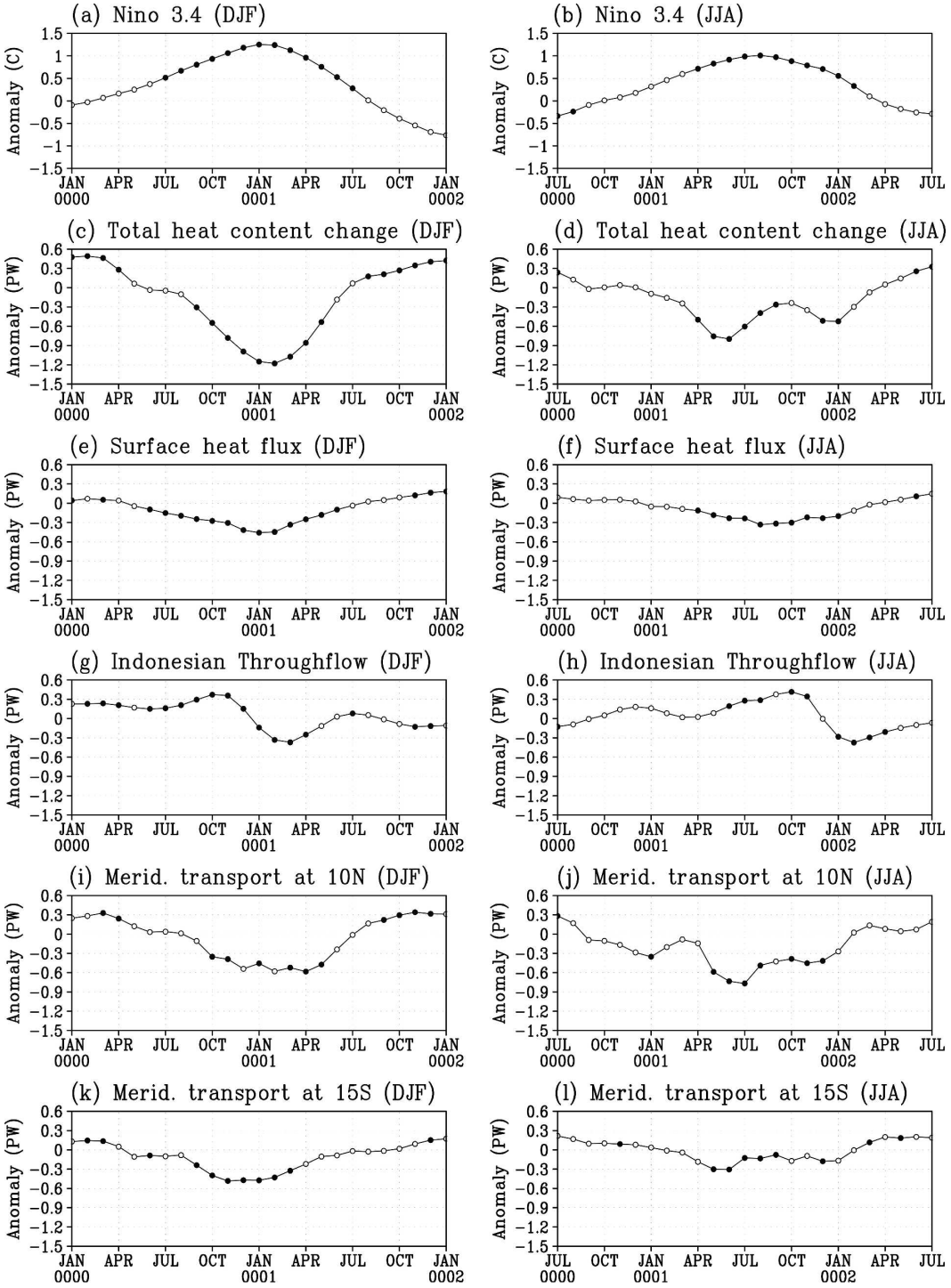

FIG. 7. Composite diagrams of anomalies: (a), (b) temperature (°C), (c), (d) total heat content change, (e), (f) surface heat flux, (g), (h) heat transport by the Indonesian Throughflow, (i), (j) meridional heat transport at 10°N, and (k), (l) meridional heat transport at 15°S for (left) winter and (right) summer El Niño–like events [(c)–(l) in PW] for a 2-yr period centered around their peak. Filled circles signify that anomalies are statistically significant at 95% confidence level.

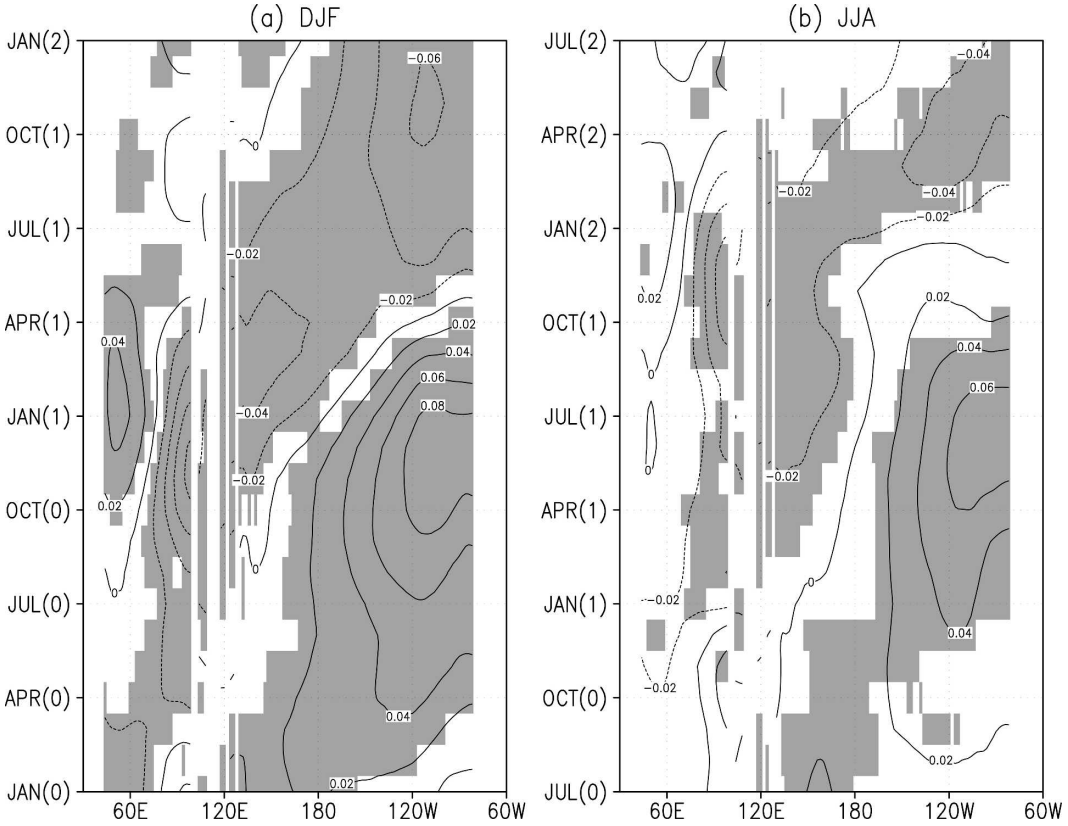

FIG. 8. Composite time–longitude cross sections of SSHA along the equator in the Indian and Pacific Oceans for (a) winter and (b) summer El Niño–like events. Contour interval is 0.02 m. Shading indicates anomalies exceeding 95% confidence level.

bifurcation latitude is consistent with an OGCM study of Qu et al. (2004). We note that the seasonal dependence may be explained by the seasonal march of the bifurcation latitude (figure not shown); it is located at the southernmost (northernmost) latitude during boreal summer (winter). The tendency for the western boundary current to compensate for the changes in the interior transport is also in agreement with previous OGCM studies (e.g., Capotondi et al. 2005), but its seasonal dependence has never been discussed. Then, the next question is what causes the differences in the meridional heat transport anomalies among different types of El Niño–like events and between two hemispheres?

The zonal wind stress anomalies for both types of El Niño–like events are shown in Fig. 11. Westerly wind stress anomalies along the equator and easterly wind stress anomalies in the off-equatorial region are captured well. The pattern is consistent with the Rossby wave response (Matsuno 1966; Gill 1980) to increased atmospheric heating over the warmer SST. Because the convective anomaly is stronger for the winter El Niño–like event, the magnitude of the wind stress anomaly is also larger for the winter El Niño. This explains the larger poleward heat transport in the off-equatorial region by the Ekman transport in both hemispheres. It is worth noting, however, that the easterly wind stress anomalies are located around 15°S in the Southern Hemisphere, whereas it is located closer to the equator in the Northern Hemisphere.

The heat transported poleward from the tropical box influences oceanic conditions in midlatitudes through the NEC and the Kuroshio (Fig. 12). The heat transport anomaly by the Kuroshio at 25°N increases by 0.08 PW at a maximum seven months after the Niño-3.4 index reaches the peak. This is qualitatively in agreement with the earlier study by Yamagata et al. (1985) using subsurface ocean data, although the time lag suggested there was much longer (18 months). The anomaly magnitude and the time lag are almost insensitive to types of El Niño–like events. The heat transported by the Kuroshio must be released to the atmosphere in the Kuroshio Extension region. However, the process is not clear in the present model; it is masked by high atmospheric variability and cannot be detected by the composite analysis.

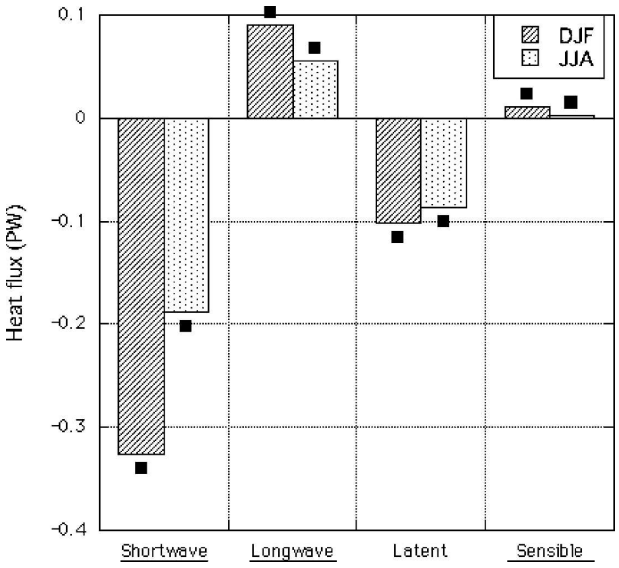

FIG. 9. Shortwave radiation, longwave radiation, latent heat, and sensible heat anomalies (PW) for the winter and summer El Niño–like events. Positive anomalies signify that ocean gains heat. A black square near a bar indicates that the anomaly is statistically significant at 95% confidence level when tested by the *t* test. An underline beneath the names of the anomalies at the bottom of the figure indicates that the difference in anomalies is statistically significant at 95% confidence level when tested by the *t* test.

5. Conclusions

Using outputs from 200-yr integration of the SINTEX-F1 ocean–atmosphere coupled model, we have investigated thermodynamical aspects of the simulated ENSO events by introducing a seasonal viewpoint. All ENSO-like events are classified into four types based on their peak season. It is shown that the tropical Pacific loses more heat for the events peaking in winter compared with the events peaking in summer, in agreement with the analysis of assimilation data. This feature is robust against changes in the meridional extent of the analysis; although they were set at 15°S and 10°N in the present study, we obtained qualitatively the same result, even when we shifted them within 15° of the equator in both hemispheres. The surface heat flux, the southward heat transport at 15°S, and the Indonesian Throughflow heat transport contribute constructively to this remarkable seasonal difference.

The Indonesian Throughflow supplies anomalous heat from the Indian Ocean, especially during the summer El Niño–like event. The influence on the recharge–discharge oscillator in the tropical Pacific from the Indian Ocean through the Indonesian Throughflow is our novel aspect.

The off-equatorial southward heat transport export is more active during the winter El Niño–like events; major contribution comes from the Ekman heat transport. North of 5°S, the Ekman heat transport is equatorward and stronger during the winter El Niño–like events owing to the stronger westerly wind stress anomaly near the equator (Fig. 11). However, the interior geostrophic heat transport is also significantly stronger and poleward for the winter El Niño–like events. Moreover, the heat transported poleward from the tropical box also affects the oceanic condition in the midlatitude through

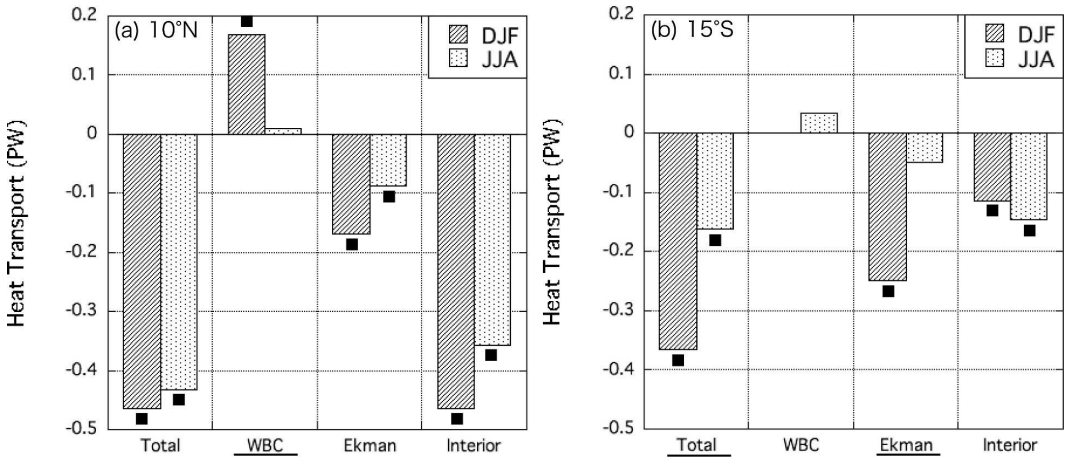

FIG. 10. Total, Ekman, western boundary current (WBC), and interior geostrophic heat transport anomalies (PW) for the winter and summer El Niño-like events at (a) 10°N and (b) 15°S. Positive anomalies signify an equatorward heat transport. A dot near a bar indicates that the anomaly is statistically significant at 95% confidence level when tested by *t* test. An underline beneath the names of the anomalies at the bottom of the figure indicates that the difference in anomalies is statistically significant at 95% confidence level when tested by the *t* test. A black square near a bar indicates that the anomaly is statistically significant at 95% confidence level when tested by a *t* test.

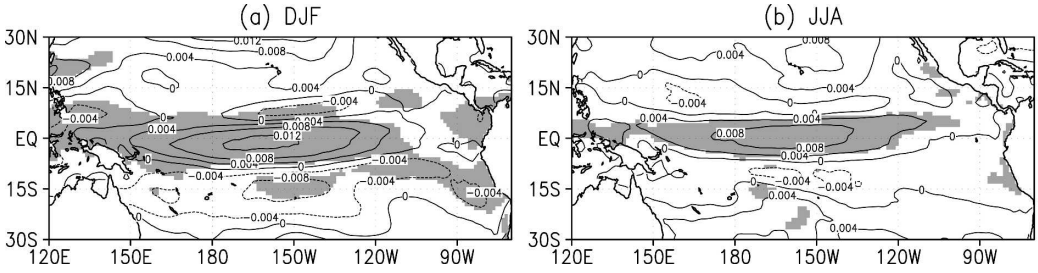

FIG. 11. Composite diagrams of zonal wind stress anomaly at the peak phase of (a) winter and (b) summer El Niño–like events. Contour interval is 0.004 N m^{-2}. Shading indicates anomalies exceeding 95% confidence level.

the NEC and the Kuroshio; the heat transport by the Kuroshio at 25°N increases by 0.08 PW at a maximum seven months after the Niño-3.4 index reaches the peak.

Although we have calculated anomalies by simply subtracting the monthly climatology, another approach is possible. For example, anomalies may also be divided into the interannual variability, modulations in the seasonal cycle, and the intraseasonal variability, including the effect of tropical instability waves (Pezzulli et al. 2005; Vialard et al. 2001). It is interesting to examine how they interact. This is because the amplitude of the seasonal cycle is known to vary both with the interannual ENSO and the decadal variability (Tozuka and Yamagata 2003; Pezzulli et al. 2005). The activity of tropical instability waves also varies with the seasonal cycle and under the influence of the interannual ENSO (Johnson and Proehl 2004). These phenomena with interactions should be addressed with a higher-resolution OGCM.

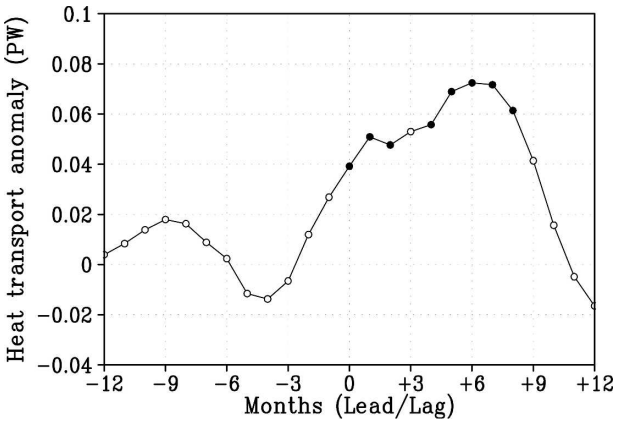

FIG. 12. Composite diagram of the meridional heat transport anomaly (PW) by the Kuroshio at 25°N for all El Niño–like events. Positive anomalies signify northward anomalies and filled circles signify that anomalies are statistically significant at 95% confidence level.

The present seasonally stratified analysis of the recharge–discharge oscillator is based on the CGCM results. To check this hypothesis, more observational data, especially the subsurface ocean data, are certainly necessary.

Acknowledgments. We thank Drs. G. Philander, R. Lukas, S.-I. An, and T. Miyasaka for stimulating discussions. We are indebted to Dr. R. Zhang for data management. The SINTEX-F1 model was run on the Earth Simulator. The present research is supported by the twenty-first-century COE grant for the "Predictability of the Evolution and Variation of the Multi-scale Earth System: An Integrated COE for Observational and Computational Earth Science" of the University of Tokyo (Leader: T. Yamagata) from the Ministry of Education, Culture, Sports, Science, and Technology of Japan, and the Japan Society for Promotion of Science through Grant-in-Aid for Young Scientists (B).

APPENDIX

Ekman Heat Transport

The meridional Ekman heat transport (cf. Kundu 1990; Sato and Polito 2005) is calculated by

$$\mathrm{EHT} = -c_p \int_0^L \frac{\tau^x}{f} T_e \, dx, \tag{A1}$$

where c_p is the specific heat of seawater (4100 J kg^{-1} K^{-1}), L is the width of the basin, τ^x is the zonal wind stress, f is the Coriolis parameter, and T_e is the mean temperature of the Ekman layer. The meridional Ekman velocity is given by

$$v_n(z) \propto e^{z/\delta} \sin\left(\frac{-z}{\delta} + \frac{\pi}{4}\right), \tag{A2}$$

where δ is the depth of the Ekman layer and it is assumed to be a constant (50 m). The velocity weights are estimated for the model depths of $z = -5, -15, -25,$

TABLE A1. Velocity weights used to calculate mean velocity-weighted temperature in the Ekman layer.

z (m)	−5	−15	−25	−35	−45	−55	−65.1	−75.1	−85.3	−95.5
$v_n(z)$	0.187	0.176	0.156	0.133	0.108	0.085	0.063	0.045	0.029	0.017

−35, −45, −55, −65.1, −75.1, −85.3, and −95.5 m and are normalized. The 10 coefficients thus obtained are shown in Table A1. Then, the mean velocity-weighted temperature in the Ekman layer is

$$T_e(x, y) = \sum v_n(z) T(x, y, z). \quad \text{(A3)}$$

The geostrophic heat transport is estimated as the difference between the total heat transport and the Ekman heat transport.

REFERENCES

AchutaRao, K., and K. R. Sperber, 2006: ENSO simulation in coupled ocean-atmosphere models: Are the current models better? *Climate Dyn.,* **27,** 1–15.

Battisti, D. S., and A. C. Hirst, 1989: Interannual variability in the tropical atmosphere–ocean model: Influence of the basic state, ocean geometry and nonlinearity. *J. Atmos. Sci.,* **46,** 1687–1712.

Boccaletti, G., R. C. Pacanowski, S. George, H. Philander, and A. V. Fedorov, 2004: The thermal structure of the upper ocean. *J. Phys. Oceanogr.,* **34,** 888–902.

Capotondi, A., M. A. Alexander, C. Deser, and M. J. McFadden, 2005: Anatomy and decadal evolution of the Pacific subtropical–tropical cells (STCs). *J. Climate,* **18,** 3739–3758.

England, M. H., and F. Huang, 2005: On the interannual variability of the Indonesian throughflow and its linkage with ENSO. *J. Climate,* **18,** 1435–1444.

Gill, A. E., 1980: Some simple solutions for heat-induced tropical circulation. *Quart. J. Roy. Meteor. Soc.,* **106,** 447–462.

Guilyardi, E., 2006: El Niño mean state seasonal cycle interactions in a multi-model ensemble. *Climate Dyn.,* **26,** 329–348.

——, P. Delecluse, S. Gualdi, and A. Navarra, 2003: Mechanisms for ENSO phase change in a coupled GCM. *J. Climate,* **16,** 1141–1158.

——, and Coauthors, 2004: Representing El Niño in coupled ocean–atmosphere GCMs: The dominant role of the atmospheric component. *J. Climate,* **17,** 4623–4629.

Harrison, D. E., and G. A. Vecchi, 1999: On the termination of El Niño. *Geophys. Res. Lett.,* **26,** 1593–1596.

Holland, C. L., and G. T. Mitchum, 2003: Interannual volume variability in the tropical Pacific. *J. Geophys. Res.,* **108,** 3369, doi:10.1029/2003JC001835.

Horii, T., and K. Hanawa, 2004: A relationship between timing of El Niño onset and subsequent evolution. *Geophys. Res. Lett.,* **31,** L06304, doi:10.1029/2003GL019239.

Jin, F.-F., 1997: An equatorial ocean recharge paradigm for ENSO. Part I: Conceptual model. *J. Atmos. Sci.,* **54,** 811–829.

——, J. D. Neelin, and M. Ghil, 1994: El Niño on the devil's staircase: Annual subharmonic steps to chaos. *Science,* **264,** 70–72.

Johnson, E. S., and J. A. Proehl, 2004: Tropical instability wave variability in the Pacific and its relation to large-scale currents. *J. Phys. Oceanogr.,* **34,** 2121–2147.

Kalnay, E., and Coauthors, 1996: The NCEP/NCAR 40-Year Reanalysis Project. *Bull. Amer. Meteor. Soc.,* **77,** 437–471.

Kug, J.-S., and I.-S. Kang, 2006: Interactive feedback between ENSO and the Indian Ocean. *J. Climate,* **19,** 1784–1801.

Kundu, P. K., 1990: *Fluid Mechanics*. Academic Press, 638 pp.

Lengaigne, M., J.-P. Boulanger, C. Menkes, and H. Spencer, 2006: Influence of the seasonal cycle on the termination of El Niño events in a coupled general circulation model. *J. Climate,* **19,** 1850–1868.

Luo, J.-J., S. Masson, S. Behera, S. Gualdi, A. Navarra, P. Delecluse, and T. Yamagata, 2003: South Pacific origin of the decadal ENSO-like variation as simulated by a coupled GCM. *Geophys. Res. Lett.,* **30,** 2250, doi:10.1029/2003GL018649.

Madec, G., P. Delecluse, M. Imbard, and C. Levy, 1998: OPA version 8.1 ocean general circulation model reference manual. LODYC/IPSL Tech. Rep. 11, 91 pp.

Masumoto, Y., 2002: Effects of interannual variability in the eastern Indian Ocean on the Indonesian Throughflow. *J. Oceangr.,* **58,** 175–182.

——, and T. Yamagata, 1991: On the origin of a model ENSO in the western Pacific. *J. Meteor. Soc. Japan,* **69,** 197–207.

Matsuno, T., 1966: Quasi-geostrophic motions in the equatorial area. *J. Meteor. Soc. Japan,* **44,** 25–43.

Meinen, C. S., and M. J. McPhaden, 2000: Observations of warm water volume changes in the equatorial Pacific and their relationship to El Niño and La Niña. *J. Climate,* **13,** 3551–3559.

Meyers, G., 1996: Variation of Indonesian throughflow and the El Niño-Southern Oscillation. *J. Geophys. Res.,* **101,** 12 255–12 263.

Neelin, J. D., D. S. Battisti, A. C. Hirst, F.-F. Jin, Y. Wakata, T. Yamagata, and S. Zebiak, 1998: ENSO theory. *J. Geophys. Res.,* **103,** 14 261–14 290.

Pezzulli, S., D. B. Stephenson, and A. Hannachi, 2005: The variability of seasonality. *J. Climate,* **18,** 71–88.

Philander, S. G. H., and R. C. Pacanowski, 1986: The mass and heat budget in a model of the tropical Atlantic Ocean. *J. Geophys. Res.,* **91,** 14 212–14 220.

Qu, T., Y. Y. Kim, M. Yaremchuk, T. Tozuka, A. Ishida, and T. Yamagata, 2004: Can Luzon Strait transport play a role in conveying the impact of ENSO to the South China Sea? *J. Climate,* **17,** 3644–3657.

Rasmusson, E. M., and T. H. Carpenter, 1982: Variations in tropical sea surface temperature and surface wind fields associated with the Southern Oscillation/El Niño. *Mon. Wea. Rev.,* **110,** 354–384.

Reid, J. L., 1997: On the total geostrophic circulation of the Pacific Ocean: Flow patterns, tracers, and transports. *Prog. Oceanogr.,* **39,** 263–352.

Roeckner, E., and Coauthors, 1996: The atmospheric general circulation model ECHAM4: Model description and simulation of present day climate. Max-Plank-Institut für Meteorologie Rep. 218, 90 pp.

Saji, N. H., B. N. Goswami, P. N. Vinayachandran, and T. Yamagata, 1999: A dipole mode in the tropical Indian Ocean. *Nature,* **401,** 360–363.

Sato, O. T., and P. S. Polito, 2005: Comparison of the global meridional Ekman heat flux estimated from four wind sources. *J. Phys. Oceanogr.,* **35,** 94–108.

Schopf, P. S., and M. J. Suarez, 1988: Vacillations in a coupled ocean–atmosphere model. *J. Atmos. Sci.,* **45,** 549–566.

Smith, T. M., and R. W. Reynolds, 2003: Extended reconstruction of global sea surface temperatures based on COADS data (1854–1997). *J. Climate,* **16,** 1495–1510.

Stammer, D., and Coauthors, 2003: Volume, heat, and freshwater transports of the global ocean circulation 1993–2000, estimated from a general circulation model constrained by World Ocean Circulation Experiment (WOCE) data. *J. Geophys. Res.,* **108,** 3007, doi:10.1029/2001JC001115.

Talley, L. D., 2003: Shallow, intermediate, and deep overturning components of the global heat budget. *J. Phys. Oceanogr.,* **33,** 530–560.

Tozuka, T., and T. Yamagata, 2003: Annual ENSO. *J. Phys. Oceanogr.,* **33,** 1564–1578.

——, J.-J. Luo, S. Masson, S. K. Behera, and T. Yamagata, 2005: Simulated annual ENSO in a coupled ocean-atmosphere model. *Dyn. Atmos. Oceans,* **39,** 41–60.

——, J.-J. Luo, S. Masson, and T. Yamagata, 2007: Decadal modulations of the Indian Ocean dipole in the SINTEX-F1 coupled GCM. *J. Climate,* **20,** 2881–2894.

Tziperman, E., L. Stone, M. A. Cane, and H. Jarosh, 1994: El Niño chaos: Overlapping of resonances between the seasonal cycle and the Pacific ocean-atmosphere oscillator. *Science,* **264,** 72–74.

——, S. E. Zebiak, and M. A. Cane, 1997: Mechanisms of seasonal–ENSO interaction. *J. Atmos. Sci.,* **54,** 61–71.

Valcke, S., L. Terray, and A. Piacentini, 2000: The OASIS coupler user guide version 2.4. CERFACS Tech. Rep. TR/CMGC/00-10, 85 pp.

Vialard, J., C. Menkes, J.-P. Boulanger, P. Delecluse, E. Guilyardi, M. J. McPhaden, and G. Madec, 2001: A model study of oceanic mechanisms affecting equatorial Pacific sea surface temperature during the 1997–98 El Niño. *J. Phys. Oceanogr.,* **31,** 1649–1675.

Weisberg, R. H., and C. Wang, 1997: A western Pacific oscillator paradigm for the El Niño-Southern Oscillation. *Geophys. Res. Lett.,* **24,** 779–782.

Wyrtki, K., 1975: El Niño—The dynamic response of the equatorial Pacific Ocean to atmospheric forcing. *J. Phys. Oceanogr.,* **5,** 572–584.

——, 1985: Water displacements in the Pacific and the genesis of El Niño cycles. *J. Geophys. Res.,* **90,** 7129–7132.

Xu, J., and J. C. L. Chan, 2001: The role of the Asian–Australian monsoon system in the onset time of El Niño events. *J. Climate,* **14,** 418–433.

Yamagata, T., Y. Shibao, and S. Umatani, 1985: Interannual variability of the Kuroshio Extension and its relation to the Southern Oscillation. *J. Oceanogr. Soc. Japan,* **41,** 274–281.